JACS
JOURNAL OF THE AMERICAN CHEMICAL SOCIETY
pubs.acs.org/JACS
Article

Rational Design of Light-Driven Molecular Motors Enabled by a Data-Efficient Machine Learning Framework for Nonadiabatic Dynamics

Jianzheng Ma, Chenwei Jiang, Lei Peng, Yongliang Shi, Yingzhou Li, Zhenggang Lan, Oleg V. Prezhdo, Xin-Gao Gong, and Weibin Chu*

Cite This: J. Am. Chem. Soc. 2026, 148, 34758−34770

ABSTRACT: Light-driven molecular rotary motors convert photon energy into mechanical motion, but designing systems that combine high rotational speed with robust unidirectionality remains a fundamental challenge. Conventional four-stroke motors rely on thermally activated steps that often slow complete rotary cycles to microsecond-to-second or even longer time scales, whereas emerging bioinspired designs may achieve much faster photoinduced rotation. However, the computational study of both classes is limited by the prohibitive cost of quantum-chemical nonadiabatic dynamics over the extended time scales required to resolve productive rotary motion. Here, we introduce N^{2}ZND, a Neural Network Zhu−Nakamura Dynamics framework that combines hierarchical sampling with E(3)-equivariant deep learning to enable data-efficient simulations of excited-state molecular motor dynamics. Trained on sparse, chemically targeted high-level ab initio data, N^{2}ZND achieves chemical accuracy and enables extensive nonadiabatic simulations of light-driven motors across relevant time scales. Application of N^{2}ZND to a complex bioinspired motor reveals a two-stroke operating mechanism that bypasses the thermally activated barriers characteristic of conventional four-stroke motors, enabling complete rotary motion on a picosecond time scale. We further identify an intrinsic speed-directionality trade-off: removal of thermal gating accelerates rotation but can reduce directional fidelity through excited-state wavepacket bifurcation. Guided by this mechanistic insight, we rationally designed a structurally modified motor in which steric tuning reshapes the excited-state topology, restoring robust room-temperature unidirectionality while preserving picosecond rotary operation. These results establish N^{2}ZND as a scalable platform for mechanistic discovery and rational design of light-driven molecular machines, providing a foundation for future high-throughput screening across traditional and bioinspired motor architectures.

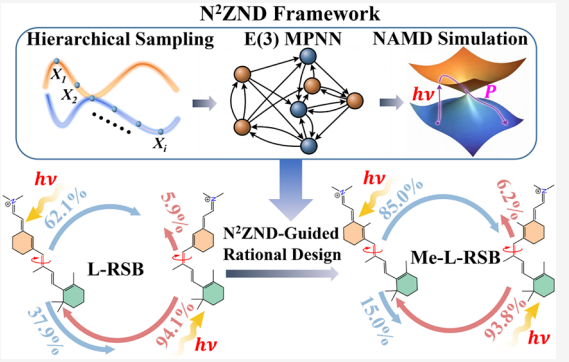

INTRODUCTION

Light-driven molecular rotary motors (LDMRMs) are sophisticated nanoscale machines capable of converting light energy into unidirectional mechanical work, holding immense potential for next-generation smart materials and nanotechnology.[1−6] The intricate operation of these devices is governed by photoisomerization, an ultrafast transformation that is inherently nonadiabatic, driven by the breakdown of the Born−Oppenheimer approximation at conical intersections (ConIs), where electronic and nuclear dynamics become inextricably coupled. Consequently, elucidating the mechanistic details and rationally designing highly efficient motors requires nonadiabatic molecular dynamics (NAMD) simulations capable of tracking atomic motion with high fidelity. For complex polyatomic systems involving large-amplitude nuclear motion and extensive nonadiabatic couplings, Trajectory Surface Hopping (TSH) combined with on-the-fly electronic structure calculations has emerged as the most practical approach.[7−11] However, the widespread application of TSH is severely hindered by a computational dilemma regarding the underlying electronic structure methods. Accurately resolving the topology of ConIs typically demands high-level multireference methods (e.g., CASSCF and CASPT2), which are computationally prohibitive given the need to perform millions of gradient evaluations to propagate a statistically meaningful ensemble of trajectories for large systems or extended time scales.[12,13] Conversely, efficient single-reference methods like Time-Dependent Density Functional Theory (TDDFT) often yield qualitatively incorrect topologies near intersections. This prohibitive cost of reliable

Received: May 18, 2026
Revised: July 24, 2026
Accepted: July 27, 2026
Published: August 4, 2026

on-the-fly calculations remains a formidable barrier, leaving the functional dynamics of complex molecular motors—such as emerging bioinspired architectures[14]—largely unexplored.

Recently, Machine Learning (ML) has emerged as a transformative approach to circumvent these computational bottlenecks by constructing surrogate potential energy surfaces (PESs).[12,15,16] Yet, a profound disparity remains between the maturity of ML for ground-state versus excited-state regimes. While ML force fields now routinely accelerate ground-state dynamics to *ab initio* accuracy, excited-state dynamics present a fundamentally more challenging problem. Unlike the smooth, single-valued landscape of the ground state, excited-state dynamics occur on a manifold of intersecting surfaces characterized by singularities and nonadiabatic couplings (NACs). Learning this complex global topology is far more demanding than fitting a single adiabatic surface. Consequently, despite architectural advances,[17−23] current ML-NAMD workflows suffer from severe data inefficiency. Training a robust model typically requires 10^4−10^5 high-level quantum chemical calculations,[17−23] forcing an undesirable compromise between using computationally affordable but inaccurate methods (e.g., TDDFT) or accepting that high-level multireference data cannot be generated in sufficient volume. Furthermore, the direct learning of NACs is notoriously difficult and prone to numerical instability, creating a significant barrier to stable long-time simulations. To address this challenge, recent strategies have sought to robustly learn NACs using advanced architectures,[20,22−24] derive them indirectly from machine-learned Hamiltonians,[25−28] or circumvent explicit NACs entirely via diabatic representations or probability-based approximations.[18,21,29,30]

Here, we present N^2ZND (Neural Network Zhu−Nakamura Dynamics), a framework designed to overcome the accuracy-cost trade-off in simulating molecular motors through very high data efficiency. Our approach integrates three synergistic strategies. First, we employ Mixed-Reference Spin-Flip TDDFT (MRSF-TDDFT)[31−34] as the reference electronic structure method. Unlike standard TDDFT, which fails to describe ConIs correctly, and conventional SF-TDDFT, which suffers from spin contamination, MRSF-TDDFT provides a spin-pure, balanced description of ConIs and strong non-dynamic correlation without the prohibitive scaling of multireference methods.[34,35] Second, we implement a Hierarchical On-the-Fly sampling strategy to achieve very high data efficiency. By utilizing efficient semiempirical OM2/MRCI trajectories,[36−40] (four to 6 orders of magnitude faster than *ab initio* methods) for broad phase-space exploration, followed by targeted MRSF-TDDFT refinement, we train E(3)-equivariant Allegro models[41] to chemical accuracy using sparse data sets of only ∼1000 points, which is orders of magnitude fewer than conventional approaches. Third, we bypass the complexities of NAC prediction entirely by adopting the Zhu−Nakamura (ZN) method,[42−44] which computes hopping probabilities directly from the scalar potential energy landscape.

We demonstrate the power of N^2ZND through its comprehensive application to LDMRMs, progressing from fundamental photoisomerization benchmarks to the elucidation and rational design of complex bioinspired architectures. Initial benchmarks on CH_2NCH_3 confirm that N^2ZND accurately reproduces full *ab initio* branching ratios and decay lifetimes. Next, in the study of the oxindole-based DDIYM motor,[45−47] the framework captures subtle pyramidalization distortions at ConIs and precise energetics of ground-state thermal helix inversion (THI) steps that elude standard methods. Finally, applying N^2ZND to a complex bioinspired L-RSB motor[14] reveals a novel, highly efficient two-stroke rotation mechanism driven by pure axial rotation that completely bypasses slow thermal helix inversion steps, a discovery made possible by the framework's ability to perform long-time scale (20−100 ps) nonadiabatic simulations at *ab initio* accuracy. Crucially, our extended simulations uncover an intrinsic trade-off between operational speed and rotational unidirectionality in these motors: the elimination of ground-state thermal barriers—which traditionally act as kinetic gates—facilitates wavepacket bifurcation on the excited state, thereby compromising directional control. By leveraging the efficiency of N^2ZND, we demonstrate that this limitation can be successfully overcome through rational structural design. We present a modified motor variant (Me-L-RSB) that achieves robust unidirectionality at room temperature while strictly preserving the ultrafast picosecond dynamics.

RESULTS

Theoretical Framework of the N^2ZND

As illustrated in Figure 1, the N^2ZND framework establishes a streamlined, largely automated workflow for NAMD simulations by synergistically integrating three advanced computational modules. This approach effectively overcomes the limitations of traditional methods regarding computational cost and accuracy. The workflow initiates with a high-fidelity data set generation phase (Figure 1a), which employs the Hierarchical On-the-Fly Sampling strategy. Capturing the precise topology of ConIs is critical for nonadiabatic dynamics, yet obtaining a representative distribution of these structures is challenging. Standard approaches face a fundamental dilemma: static uniform sampling (e.g., linear interpolation sampling) is

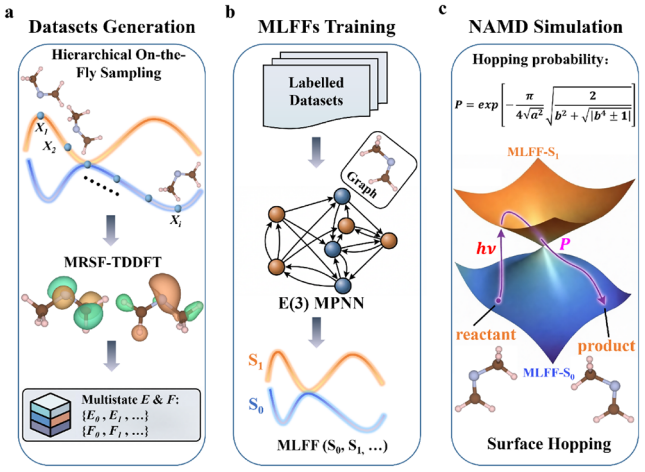

Figure 1. Integrated computational workflow of the N^2ZND framework for NAMD simulations. The pipeline comprises three synergistic modules: **a** Data sets are generated via semiempirical OM2/MRCI on-the-fly trajectories sampling, followed by high-fidelity MRSF-TDDFT single-point energy and gradient calculations to produce a refined set of only about 1000 labeled molecular configurations. **b** MLFFs for ground and excited states are trained using an E(3)-equivariant graph neural network. **c** NAMD simulations are performed via the Zhu−Nakamura surface hopping method, which computes transition probabilities (P) directly from the MLFF-based PESs (MLFF-S_0, MLFF-S_1) to model postexcitation ($h\nu$) relaxation dynamics from reactant to product.

https://doi.org/10.1021/jacs.6c10141
J. Am. Chem. Soc. 2026, 148, 34758−34770

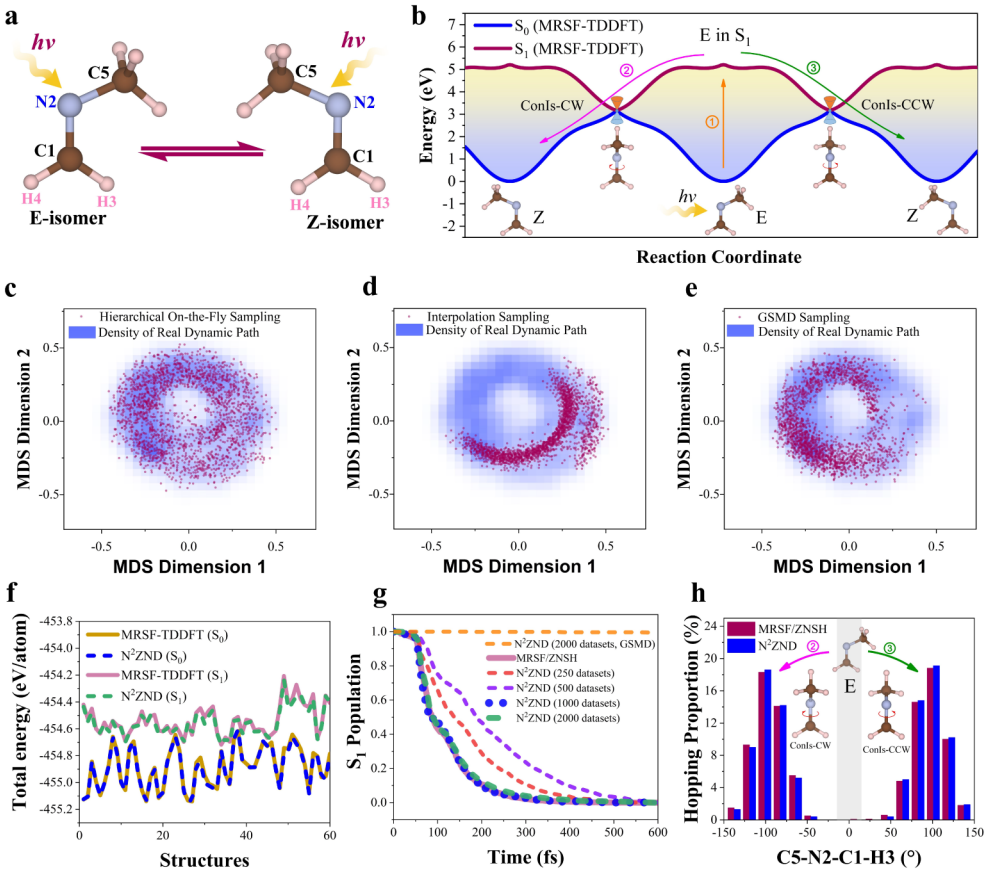

Figure 2. Computational study of the photoisomerization mechanism for CH_2NCH_3. **a** Reversible photoisomerization between the E and Z isomers. **b** Potential energy profiles for the S_0 (blue) and S_1 (red) states calculated at the MRSF-TDDFT level. The reaction mechanism is characterized by three distinct processes: ① vertical excitation from the stable E-isomer to the S_1 state, followed by relaxation toward ConIs via either ② CW or ③ CCW torsional pathways. **c**–**e** MDS analysis comparing the phase space coverage of different sampling strategies against the "Real Dynamic Path". **f** Total energy per atom for a series of molecular configurations on the S_0 and S_1 states, comparing results from MRSF-TDDFT (solid lines) and N^2ZND (dashed lines) calculations. **g** Time-dependent S_1 state population decay profiles from NAMD simulations. The plot compares the reference MRSF/ZNSH benchmark against models trained using the Hierarchical On-the-fly Sampling strategy with varying data set sizes (250, 500, 1000, and 2000), and the model trained using the GSMD sampling strategy (2000 data points). **h** Statistical distribution of hopping events versus the C5–N2–C1–H3 dihedral angle obtained from NAMD simulations using MRSF/ZNSH and N^2ZND methods. The data highlights the bifurcation of the wavepacket into the ② CW (negative angles) and ③ CCW (positive angles) decay channels.

inefficient, often introducing irrelevant high-energy configurations that pollute the model; conversely, generating training configurations via direct *ab initio* nonadiabatic molecular dynamics (NAMD) using high-level methods is computationally prohibitive, rendering it unacceptable for large systems or long-time scale simulations. To resolve this conflict, initial molecular configurations are extensively sampled via computationally efficient semiempirical OM2/MRCI on-the-fly trajectories. This dynamic exploration is crucial: it filters out irrelevant high-energy regions and focuses sampling on the actual reaction channels at a negligible cost. It should be emphasized that OM2/MRCI is used only for rapid phase-space exploration rather than for the final production NAMD simulations, because direct dynamics on OM2/MRCI PESs may yield quantitatively unreliable Zhu–Nakamura hopping probabilities when semiempirical errors affect the relevant energetics, gradients, and crossing-region gaps. These dynamically selected structures are then refined via MRSF-TDDFT single-point energy and gradient calculations. A critical advantage of this module is the deployment of MRSF-TDDFT, which provides a balanced description of strong nondynamic correlation and ConIs without the prohibitive scaling and active-space sensitivity associated with CASSCF, nor the spin contamination issues inherent to conventional SF-TDDFT.[34,35] This rigorous filtering process yields a remarkably concise data set of only approximately 1000 labeled structures, a substantial reduction in data volume that nonetheless comprehensively covers critical regions of the PES.

Leveraging these refined data sets, the workflow proceeds to the training of Machine Learning Force Fields (MLFFs) for both ground and excited states (Figure 1b). N^2ZND utilizes the Allegro model, an E(3)-equivariant graph neural network.[41] Benefiting from the synergy between the strict symmetry-preserving inductive biases of this architecture and the high physical relevance of the sampled configurations, the framework achieves predictive accuracy comparable to high-level *ab initio* calculations using such an exceptionally sparse data set. This represents a dramatic reduction in data requirements compared to conventional machine learning approaches, which typically necessitate tens of thousands of training structures.[17,18,20,23] By achieving chemical accuracy with a minimal data set, N^2ZND significantly lowers the computational barrier for modeling global PESs, facilitating

https://doi.org/10.1021/jacs.6c10141
J. Am. Chem. Soc. 2026, 148, 34758–34770

efficient structural optimizations (including local minima, transition states, and ConIs) and NAMD simulations.

Finally, the constructed potentials drive the NAMD simulations (Figure 1c), which are performed using the Zhu−Nakamura trajectory surface hopping method. Distinct from standard approaches that rely on explicit NAC, the Zhu−Nakamura method eliminates the need for expensive and numerically unstable NAC calculations, thereby enhancing both computational efficiency and numerical stability. By integrating this NAC-free approach with the smooth, accurate PES provided by the MLFFs, N^2ZND effectively captures nonadiabatic transitions and relaxation dynamics in complex photochemical systems, offering a robust solution for studying light-matter interactions in large-scale polyatomic molecules. Detailed theoretical descriptions of the MRSF-TDDFT, Allegro, Zhu−Nakamura and structural optimizations methods are all provided in the Supporting Information.

Benchmark of the N^2ZND Framework for the Photoisomerization of CH_2NCH_3

To validate the robustness of our computational strategy, we conducted a systematic comparison of NAMD simulations for *N*-methylmethanimine (CH_2NCH_3) employing the Zhu−Nakamura trajectory surface hopping methodology, utilizing two distinct approaches: N^2ZND and full *ab initio* simulations based on MRSF-TDDFT (denoted as MRSF/ZNSH). As one of the simplest Schiff bases, this molecule serves as a prototypical model for investigating photoinduced *E*−*Z* isomerization—a process involving the reversible switching between the *trans*-like (*E*) and *cis*-like (*Z*) configurations via rotation around the central C═N double bond (Figure 2a).[48] Capturing this motion requires accurately modeling the ultrafast passage through conical intersections, the points where excited and ground states meet. In order to rigorously validate the superiority of the Hierarchical On-the-Fly Sampling strategy employed in N^2ZND, we compared it against two conventional data set generation protocols: Interpolation Sampling and Ground State MD (GSMD) Sampling (see Supporting Information for detailed protocols). All data sets were capped at 2000 structures to ensure a fair comparison of data efficiency. We employed Multidimensional Scaling (MDS) to project the high-dimensional molecular phase space onto a 2D plane (see Supporting Information for details).[49,50] This allows us to visualize the coverage of each training set relative to the "Real Dynamic Path," which is represented by the kernel density estimation of 84 independent reference MRSF/ZNSH trajectories (propagated for 600 fs and sampled every 25 fs).

As shown in Figure 2c, the Hierarchical On-the-Fly Sampling strategy exhibits exceptional coverage, with the training data (red points) closely matching the density of the real dynamical path (blue density). Although OM2/MRCI may not capture the ground truth or exact conical intersection topographies perfectly, it exhibits excellent ergodicity within the high-dimensional excited-state phase space. Consequently, these low-cost trajectories successfully identify the critical excited-state reaction channels of the PES. In stark contrast, the Interpolation Sampling (Figure 2d) is confined to a narrow region of phase space, failing to capture the complex actual reaction. Similarly, while the GSMD Sampling (Figure 2e) explores a broader region than interpolation, it is fundamentally limited to the ground-state basin and fails to reach the high-energy regions associated with the S_1/S_0 ConIs. We trained MLFF using each of the three data sets to assess their performance. As detailed in Table S2, the Interpolation strategy exhibits substantial errors for both states. The GSMD strategy yields a seemingly low S_0 error; however, this apparent accuracy is misleading because sampling remains restricted to the stable equilibrium basin without reaching the critical excited-state regions, resulting in a complete failure to describe the S_1 surface. In contrast, the MLFF derived from the hierarchical on-the-fly sampling strategy achieves low prediction errors for both S_0 and S_1 states, providing the balanced accuracy necessary for modeling nonadiabatic dynamics.

Having demonstrated the superior phase space coverage of the N^2ZND strategy, we proceeded to rigorously benchmark its physical reliability against high-level quantum chemical calculations. To validate the PESs, we extracted 60 snapshots from the reference MRSF/ZNSH trajectories. As shown in Figure 2f, the S_0 and S_1 energies computed by N^2ZND exhibit excellent agreement with the reference MRSF-TDDFT values. Furthermore, we employed the trained force field to optimize the critical stationary points, specifically the ground-state and ConIs structures. The geometric parameters derived from N^2ZND match those obtained from MRSF-TDDFT, CASSCF, and OM2/MRCI with remarkable consistency (Table S3).

With the validity of the PESs confirmed, we examined the reaction mechanism and simulation setup. As illustrated in Figure 2a,b, the reaction mechanism involves three distinct processes: ① vertical excitation from the stable E-isomer to the S_1 state, followed by relaxation toward ConIs via either ② clockwise (CW) or ③ counterclockwise (CCW) torsional pathways. Given the symmetry of the planar ground state, the wavepacket is expected to bifurcate equally into CW and CCW channels, rapidly returning to the S_0 state via two symmetry-equivalent intersections (ConIs-CW and ConIs-CCW). To simulate this, initial conditions were generated via Wigner sampling based on the MRSF-TDDFT ground state frequencies,[51−53] using the wigner.py program from the SHARC software package.[54,55] We propagated 3000 trajectories for the reference MRSF/ZNSH method, the models derived from GSMD and Interpolation sampling, and N^2ZND models trained on varying data set sizes (250, 500, 1000, and 2000 structures), with a simulation time of 600 fs.

The dynamical performance and data efficiency of N^2ZND were evaluated by analyzing the excited state lifetime and decay pathways. The time-dependent population of the S_1 state is depicted in Figure 2g. The critical role of sampling strategy is immediately apparent: the model trained on the GSMD Sampling data set exhibits an extremely slow decay, with only a negligible fraction of trajectories returning to the ground state within 600 fs. The Interpolation-based model performed even worse, as NAMD simulations proved unstable and led to rapid, unphysical dissociation of the molecular structures. In stark contrast, the N^2ZND strategy demonstrates a rapid convergence of dynamical accuracy. While models trained on smaller data sets (250 and 500 points) exhibit delayed relaxation, the dynamics effectively converge at a data set size of just 1000 points. Although the 2000-point model yields a lower static validation error (Table S2), the 1000-point model already reproduces the high-level MRSF/ZNSH benchmark with high fidelity. Exponential fitting of the decay data (Figure S5) yields highly consistent lifetimes between the converged N^2ZND model (2000 data sets) and the reference MRSF/ZNSH method: 123.9 and 117.0 fs, respectively.

https://doi.org/10.1021/jacs.6c10141
J. Am. Chem. Soc. 2026, 148, 34758−34770

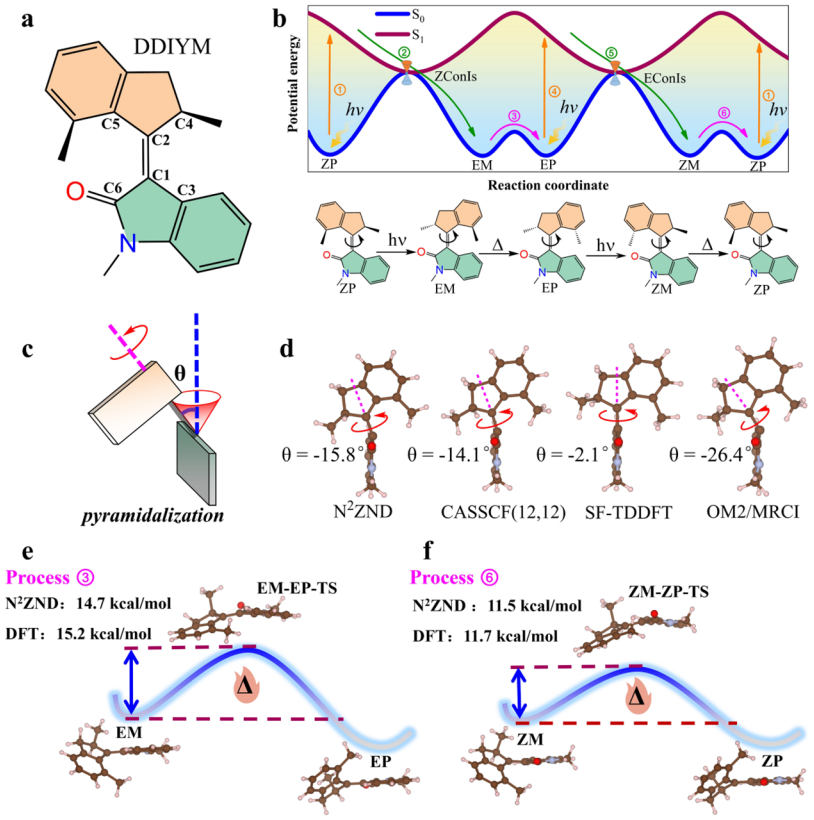

Figure 3. Mechanistic and structural characterization of the Oxindole-Based LDMRM DDIYM. **a** Chemical structure of the DDIYM molecule in its stable ZP configuration. **b** Schematic potential energy profiles for the S_0 (blue) and S_1 (red) states, illustrating the four-stroke cycle of unidirectional rotation. The sequence proceeds as follows: ① photoexcitation of ZP followed by ② nonadiabatic decay through the ZConIs to the EM isomer; ③ THI to EP; ④ second photoexcitation; ⑤ decay via the EConIs to ZM; and ⑥ final THI restoring the initial ZP state. **c** Schematic definition of the pyramidalization angle (θ), which characterizes the precessional tilting of the rotor relative to the stator. **d** Structural comparison of the Z-ConIs-1 geometry optimized at different theoretical levels. **e, f** Energy profiles for the THI steps: **e** EM → EP and **f** ZM → ZP.

Finally, we analyzed the geometric distribution of nonadiabatic transitions to verify the reaction mechanism (Figure 2h). The distribution of the C5−N2−C1−H3 dihedral angles at the hopping points clearly reveals the bifurcation of the reaction flux. Negative angles correspond to CW rotation (near ConIs-CW), while positive angles correspond to CCW rotation (near ConIs-CCW). Crucially, N^{2}ZND reproduces the statistical branching ratio of the reference method with high fidelity, exhibiting the nearly symmetric (∼1:1) bifurcation expected from the molecular symmetry. These results confirm that N^{2}ZND captures both the time scales and the mechanistic details of the photoisomerization with *ab initio* accuracy. In addition, to further establish the physical reliability of the MRSF/ZNSH scheme employed herein, a systematic comparison with Tully's fewest switches surface hopping method was performed at the same electronic structure level (denoted as MRSF/FSSH), demonstrating good agreement in both decay time scales and channel selectivity (see Figure S4 in Supporting Information for details).

Application to Oxindole-Based Light-Driven Molecular Rotary Motor

Having established the accuracy of the N^{2}ZND framework on the benchmark system, we applied it to systematically investigate the nonadiabatic dynamics of a prototype oxindole-based molecular motor, (*R*,*Z*)-3-(2,7-dimethyl-2,3-dihydro-1*H*-inden-1-ylidene)-1-methylindolin-2-one (DDIYM) (Figure 3a).[45−47]

A complete 360° rotational cycle of LDMRMs, especially Feringa-type LDMRMs, consists of four distinct steps: two photoisomerization processes and two thermal helix inversion (THI) steps.[4] The operational mechanism of DDIYM follows this general scheme. As illustrated in the potential energy profiles in Figure 3b, this cycle proceeds through a sequence of photochemical and thermal events: ① photoexcitation of the stable ZP isomer triggers a CCW rotation around the central C═C double bond; ② the system relaxes to the ground state via a conical intersection (ZConIs), yielding the metastable EM isomer; ③ a subsequent THI converts EM to the stable EP form; ④ a second photoexcitation occurs; ⑤ relaxation via EConIs produces the metastable ZM isomer; and ⑥ the isomer finally undergoes a second THI step to restore the initial ZP state.

A critical determinant of the photoisomerization efficiency in LDMRMs is the geometry of the ConIs, particularly the degree of pyramidalization at the stator-rotor linkage, as shown in Figure 3c.[46,47,56] We optimized the S_1/S_0 ConIs (Z-ConIs-1/2 and E-ConIs-1/2) using four different theoretical approaches. As shown in Figure 3c,d, the pyramidalization angle (θ, defined by the C1−C6−C3−C2 dihedral) serves as a key geometric descriptor. The values obtained from N^{2}ZND (e.g., −15.8° for Z-ConIs-1) are consistent with the CASSCF results (−14.1°), with both methods predicting significant pyramidal distortion. In stark contrast, conventional SF-TDDFT systematically underestimates this effect (−2.1°), while OM2/MRCI tends to overestimate it (−26.4°). Analogous structural trends are

https://doi.org/10.1021/jacs.6c10141
J. Am. Chem. Soc. 2026, 148, 34758−34770

Table 1. Computational Efficiency Benchmark for Single-Point Energy and Gradient Calculations on the DDIYM System[a]

	N^2ZND	OM2/MRCI	SF-TDDFT	MRSF-TDDFT	CASSCF(12,12)
Resource	1 CPU	1 CPU	64 CPUs	64 CPUs	64 CPUs
Time	0.9 s	0.6 s	2.6 min	3.9 min	4.2 h

[a]Comparison of wall-clock times required for one gradient evaluation using N^2ZND versus conventional electronic structure methods.

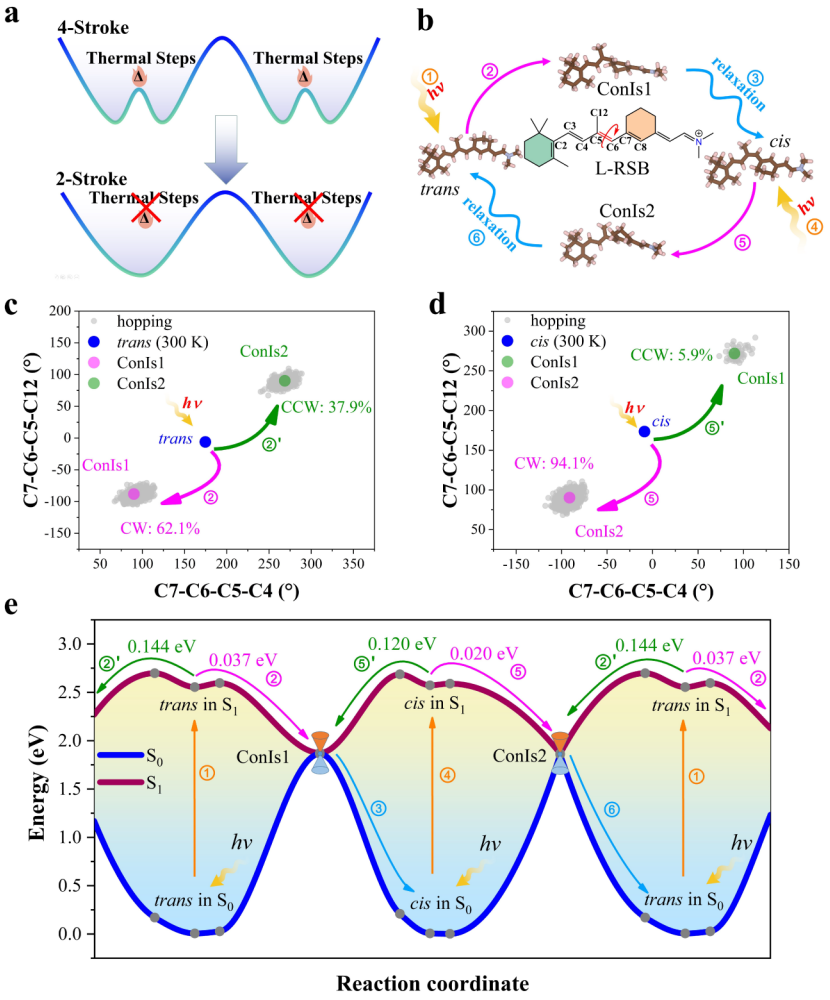

Figure 4. Mechanistic elucidation of the bioinspired L-RSB molecular motor. **a** Schematic comparison between the conventional four-stroke cycle (top) involving rate-limiting THI steps, and the efficient two-stroke cycle (bottom) of L-RSB, which bypasses THI barriers. **b** Detailed photoisomerization cycle illustrating the interconversion between the *trans* and *cis* isomers. The process proceeds as follows: ① photoexcitation of the *trans* isomer; ② nonradiative relaxation via ConIs1; ③ formation of the *cis* isomer; ④ photoexcitation of the *cis* isomer; ⑤ relaxation via ConIs2; and ⑥ return to the *trans* ground state. **c, d** Mechanistic insights from NAMD simulations at 300 K: Scatter plots of the C7−C6−C5-C4 versus C7−C6−C5−C12 dihedral angles at the hopping geometries for **c**, the *trans* → *cis* process and **d**, the *cis*→*trans* process. Reference structures and statistical distribution are marked. **e** Schematic representation of the potential energy profile of the S_0 (blue) and S_1 (red) for L-RSB along the reaction coordinate. The energies of key stationary points were computed at the MRSF-TDDFT level.

consistently observed across the other identified ConIs (Z-ConIs-2 and E-ConIs-1/2), as detailed in Supporting Information. This comparison underscores the superior ability of the N^2ZND framework to capture the subtle geometric features of ConIs that govern excited-state lifetimes and quantum yields. Comprehensive details regarding the MLFF data set construction, training metrics, and the full NAMD simulations of the DDIYM motor, including time-dependent population decay profiles, the evolution of representative trajectories, and hopping distributions, are provided in the Supporting Information. The simulation results reveal that both the ZP → EM and EP → ZM photoisomerization processes occur on an ultrafast femtosecond time scale (Figure S8), with the rotational unidirectionality reaching 100% (Figure S9).

Beyond the excited state, we also evaluated the model's ability to describe ground-state dynamics, specifically the thermal helix inversion steps. We located the transition states for the EM → EP and ZM → ZP conversions using the nudged elastic band (NEB) method refined by the FIRE optimizer,[57,58] and their ground-state single-point energies were subsequently calculated with MRSF-TDDFT. As depicted in Figure 3e,f, the THI barriers predicted by N^2ZND are 14.7 and 11.5 kcal/mol, respectively, which are in outstanding agreement with benchmark DFT calculations (15.2 and 11.7 kcal/mol).[47]

https://doi.org/10.1021/jacs.6c10141
J. Am. Chem. Soc. 2026, 148, 34758−34770

Finally, to demonstrate the superior computational efficiency of the N^{2}ZND framework, we evaluated its performance in two distinct phases: training and prediction (Table 1). First, regarding training efficiency, conventional sampling strategies typically require propagating NAMD trajectories using expensive high-level theory to harvest relevant geometries. N^{2}ZND circumvents this bottleneck through its Hierarchical On-the-Fly Sampling strategy, which decouples exploration from labeling. We utilized the ultrafast semiempirical OM2/MRCI method (0.6 s/gradient) to extensively explore the geometric phase space, followed by high-fidelity labeling using MRSF-TDDFT. As shown in Table 1, MRSF-TDDFT offers an optimal balance for this data set construction, matching CASSCF quality while running ∼65 times faster (4.2 CPU-hours vs 270 CPU-hours per gradient). This hierarchical approach ensures high data efficiency, generating a robust data set without the prohibitive cost of full *ab initio* trajectory propagation. Second, regarding prediction efficiency, the trained N^{2}ZND model delivers massive acceleration by bypassing the iterative solution of the electronic Schrödinger equation. The model achieves an inference speed of 0.9 s on a single core, representing an acceleration of approximately 4 to 6 orders of magnitude compared to the *ab initio* methods (MRSF-TDDFT and CASSCF) otherwise required for dynamics. By retaining *ab initio* accuracy at a cost comparable to semiempirical methods, N^{2}ZND effectively overcomes the computational bottlenecks that typically restrict long-time scale NAMD simulations.

Application to Bioinspired Light-Driven Molecular Rotary Motor

It is well established that the operation of conventional LDMRMs relies on a four-stroke cycle comprising two fast photoisomerization steps and two slow THI steps.[4] Since these thermal processes typically occur on microsecond-to-second or even longer time scales, they constitute the rate-determining bottleneck for the motor's rotational frequency. Moreover, traditional motors often necessitate high-energy ultraviolet (UV) excitation, which poses photodegradation risks in sensitive environments. Consequently, developing next-generation molecular machines that are capable of high-speed operation and driven by visible light has become a primary objective.[4,47,59]

To address this, a novel class of bioinspired molecular motors, designated as L-RSB, has been developed through a biomimetic engineering of the retinal protonated Schiff base backbone.[14] This chromophore has been experimentally synthesized and characterized by gas-phase time-resolved action spectroscopy, which demonstrated ultrafast excited-state dynamics on a picosecond time scale. These synthetic chromophores are distinguished by their ability to achieve unidirectional 360° rotation through a highly efficient two-stroke cycle, driven solely by two photochemical steps (Figure 4a). This mechanism effectively bypasses the rate-limiting THI processes inherent to traditional designs. Furthermore, the operational wavelength of L-RSB is significantly red-shifted away from the ultraviolet region, thereby reducing photodegradation risks and enhancing biocompatibility. This unique combination of high-speed operation and noninvasive excitation renders L-RSB particularly promising for applications in soft matter engineering and biomedical systems, where traditional motors are often constrained by speed limits and UV toxicity. However, characterizing the complete non-adiabatic operational cycle of this complex bioinspired system poses a formidable computational challenge. Its intricate biomimetic architecture entails a substantial system size and a high-dimensional configuration space, while the relaxation process extends over a picosecond time scale. These factors render standard *ab initio* on-the-fly dynamics computationally intractable. To overcome this bottleneck, we employed the N^{2}ZND framework to conduct a comprehensive mechanistic study, leveraging its high efficiency to capture the complete relaxation processes with quantum chemical accuracy.

The reaction mechanism was first established by optimizing critical stationary points using N^{2}ZND. As illustrated in Figure 4b, the reaction mechanism is characterized by six distinct processes: ① photoexcitation of the *trans* isomer initiates the cycle; ② nonradiative relaxation occurs via ConIs1; ③ the metastable *cis* isomer is formed; ④ the *cis* isomer undergoes photoexcitation; ⑤ the system decays through ConIs2; and ⑥ the *trans* ground state is finally restored. With the reaction mechanism established, we proceeded to NAMD simulations using the trained MLFFs (detailed sampling protocols and training metrics are provided in the Supporting Information). Initial conditions for the NAMD simulations were generated from ground-state molecular dynamics trajectories. After thermal equilibration in the NVT ensemble at 300 K, initial configurations and velocities were sampled at 20 fs intervals. We propagated 1000 trajectories for both the *trans* → *cis* and *cis* → *trans* transitions for 20 ps.

The dynamical mechanism was elucidated by analyzing the geometric distribution of hopping events. Figure 4c,d display scatter plots of the key dihedral angles (C7−C6−C5−C4 vs C7−C6−C5−C12) at the $S_1 \rightarrow S_0$ transition points at 300 K. For the *trans* → *cis* process (Figure 4c), the wavepacket bifurcates, with 62.1% of trajectories relaxing via ConIs1 (clockwise rotation, Process ②) and 37.9% via ConIs2 (counterclockwise, Process ②′). In contrast, the reverse *cis* → *trans* process (Figure 4d) exhibits a highly specific pathway, with 94.1% of trajectories proceeding via ConIs2 (clockwise, Process ⑤), indicating a strong unidirectional preference. Notably, structural analysis of the ConIs reveals that the pyramidality dihedral (C5−C12−C4−C6) remains near 0° (Table S8), indicating that, unlike Feringa-type motors or the DDIYM system discussed previously, the rotation of L-RSB is driven by pure axial motion around the C5═C6 bond rather than pyramidalization. Additional NAMD simulation results, including time-dependent population decay profiles and the evolution of representative trajectories, are presented in the Supporting Information. The simulation results confirm that both the *trans* → *cis* and *cis* → *trans* photoisomerization processes proceed on an ultrafast picosecond time scale (Figure S12).

To provide a quantitative energetic basis for this motion, we constructed the potential energy profiles along the reaction coordinate (Figure 4e). Stationary points on the S_1 surface, including Franck−Condon regions (*trans*-S_1, *cis*-S_1) and transition states leading to the ConIs, were optimized using N^{2}ZND. The computed energy barriers rationalize the dynamical findings. For the *trans* → *cis* transition, the barrier for the clockwise pathway (via ConIs1, Process ②) is 37 meV, significantly lower than the 144 meV barrier for the counterclockwise path (Process ②′). This energetic preference drives the observed majority flux (62.1%) into the clockwise channel. In the reverse *cis* → *trans* process, the disparity is even more pronounced: the clockwise barrier (via ConIs2, Process

https://doi.org/10.1021/jacs.6c10141
J. Am. Chem. Soc. 2026, 148, 34758−34770

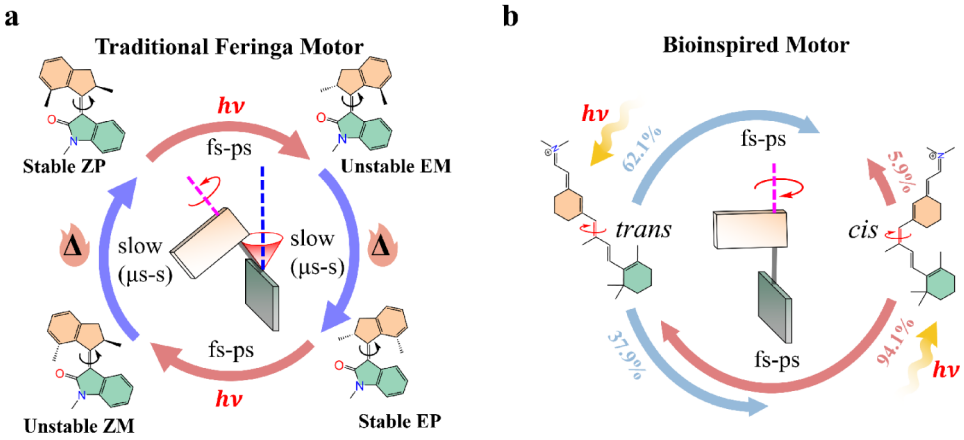

Figure 5. Mechanistic comparison between traditional and bioinspired molecular motors. **a** The traditional Feringa-type motor operates via a four-stroke cycle comprising two ultrafast photoisomerization steps and two rate-limiting THI steps. The central schematic illustrates the precessional motion. **b** The bioinspired L-RSB motor functions through a highly efficient two-stroke cycle driven exclusively by light, effectively bypassing the THI barriers. The central schematic depicts the pure axial rotation mode.

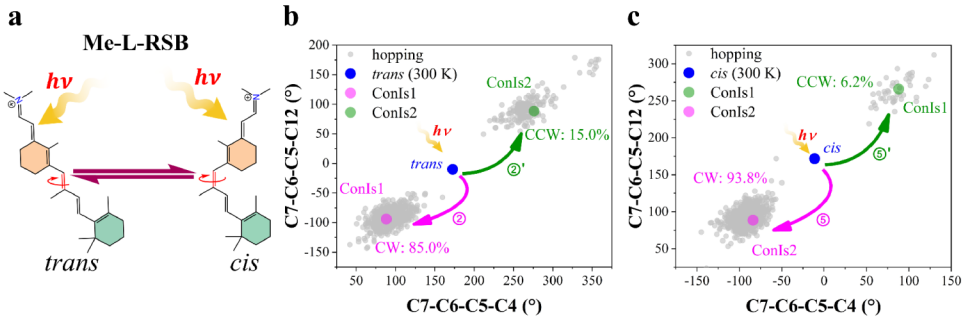

Figure 6. Mechanistic elucidation of the structurally modified bioinspired motor, Me-L-RSB. **a** Chemical structure and reversible photoisomerization cycle between the *trans* and *cis* isomers of Me-L-RSB. **b, c** Mechanistic insights from NAMD simulations at 300 K: Scatter plots of the C7−C6−C5−C4 versus C7−C6−C5−C12 dihedral angles at the hopping geometries for **b**, the *trans* → *cis* process and **c**, the *cis* → *trans* process.

⑤) is merely 20 meV, whereas the counterclockwise barrier (Process ⑤′) is 120 meV. This 6-fold difference results in almost exclusive clockwise rotation (94.1%). Collectively, these results characterize L-RSB as an excited-state-barrier-controlled two-stroke motor that exhibits high unidirectionality in the *cis* → *trans* step, but only partial directionality in the *trans* → *cis* step.

Strategies for Enhancing Unidirectionality of the Bioinspired Light-Driven Molecular Rotary Motor

The extended time scales and statistical depth provided by N^2ZND offer a vital means to investigate the mechanisms of photoisomerization, which inherently involves large atomic scales and extended simulation times. It is precisely this capability that enabled us to resolve the complex reaction coordinates and elucidate the fundamental differences between traditional Feringa-type motors and the biomimetic L-RSB system (Figure 5). Traditional motors operate through a four-stroke cycle controlled by a rate-limiting THI step, while the biomimetic motor operates through a highly efficient two-stroke cycle driven solely by photon absorption. This mechanism bypasses thermal energy barriers, enabling ultrafast dynamics characterized by purely axial rotation, rather than the precessional motion common in four-stroke systems.

However, our findings indicate that this elimination of ground-state thermal barriers introduces an intrinsic trade-off between operational speed and directionality. In the four-stroke cycle, thermal barriers act as strict kinetic gates, ensuring near-perfect unidirectionality. In contrast, the barrier-free ground-state landscape of the two-stroke motor facilitates wavepacket bifurcation, resulting in dominant but not exclusive unidirectionality (e.g., 62.1% for the *trans* → *cis* transition at 300 K).

To investigate whether this bifurcation could be suppressed, we first explored a thermodynamic control strategy. NAMD simulations of the L-RSB motor for the *trans* → *cis* process at reduced temperatures revealed that cooling the system to 150 K increases the clockwise unidirectionality to 75.5%, and further cooling to 50 K successfully restricts the counter-clockwise pathway, achieving a near-perfect 99.0%. By drastically reducing the thermal kinetic energy, the wavepacket becomes strictly confined by the subtle S_1 energy barriers. However, operating at such extreme cryogenic temperatures fundamentally defeats the purpose of developing bioinspired molecular machines. These devices are intended to function in ambient, biological, or soft-matter environments at room temperature. While thermodynamic control is effective, relying on such extreme environmental cooling is often unsuitable for real-world applications. More detailed dynamical analyses regarding the temperature effects are provided in the Supporting Information.

To achieve robust unidirectionality at room temperature (300 K), we turned to rational structural design. We

https://doi.org/10.1021/jacs.6c10141
J. Am. Chem. Soc. 2026, 148, 34758−34770

hypothesized that the topology of the excited-state potential energy surface could be rationally modulated to steer the wavepacket. To validate this, we designed and investigated a structurally modified bioinspired motor, designated as Me-L-RSB (Figure 6a), which incorporates specific steric modifications to the rotor backbone by introducing a methyl group at the C8 position (Figure 4b).

The NAMD simulations of Me-L-RSB at 300 K, enabled by the N^{2}ZND framework, notably confirm the success of this structural strategy. As illustrated in the hopping distribution plots (Figure 6b,c), the structural modification significantly alters the reaction flux. For the *trans* → *cis* transition (Figure 6b), the wavepacket is now strongly funneled into the clockwise channel (via ConIs1), achieving a highly dominant unidirectionality of 85.0%, a substantial enhancement over the unmodified L-RSB. The reverse *cis* → *trans* process (Figure 6c) maintains an exceptional clockwise directionality of 93.8%. Crucially, this enhanced control is achieved while strictly preserving the ultrafast picosecond-scale operational speed characteristic of the two-stroke mechanism at room temperature. Furthermore, MRSF-TDDFT calculations show that C8 methylation only slightly changes the $S_0 \rightarrow S_1$ vertical excitation energies at the Franck−Condon geometries (Table S13), indicating that Me-L-RSB retains essentially the same visible-light excitation window as the parent L-RSB motor. Comprehensive details for the Me-L-RSB motor, including the computational screening process, MLFF training metrics, excited-state population decay profiles, schematic potential energy profiles, excitation energy comparison, and synthetic feasibility, are provided in the Supporting Information.

DISCUSSION

The simulation of excited-state dynamics for light-driven molecular rotary motors and their rational design have long been plagued by a trade-off between cost and accuracy: accurate quantum mechanical methods are computationally too expensive over longer time scales, while efficient approximate methods often fail to capture complex nonadiabatic phenomena. The N^{2}ZND framework addresses this limitation by establishing a protocol for generating reliable excited-state machine learning potentials. By coupling Hierarchical On-the-Fly Sampling with E(3)-equivariant deep learning, we demonstrate that high accuracy can be achieved with sparse but chemically relevant data sets. Our results indicate that chemical accuracy is attainable using a concise set of strategically selected reference configurations, significantly reducing the computational overhead required to model systems of this complexity. Finally, by coupling this high-fidelity potential with the numerical stability of NAC-free surface hopping, N^{2}ZND creates a powerful approach capable of efficiently simulating complex molecular photoisomerization. Leveraging the extended simulation times and statistical depth provided by N^{2}ZND, we were able to move beyond mere observation of these motors to active rational design. We not only uncovered the intrinsic speed-directionality trade-off inherent to the bioinspired L-RSB motors but also actively resolved this limitation. By rapidly evaluating the structurally modified Me-L-RSB variant, we demonstrated that robust unidirectionality can be successfully restored via precise steric tuning of the excited-state topology, without sacrificing the signature ultrafast operational speed.

The performance of N^{2}ZND depends critically on the Hierarchical On-the-Fly Sampling strategy, which uses lower-cost nonadiabatic dynamics to explore the relevant reactive phase space before high-level labeling. In the present implementation, OM2/MRCI serves as the exploratory method. A natural concern is whether semiempirical sampling can reliably identify the important excited-state pathways. In this work, OM2/MRCI is not used as the final electronic-structure model, but rather as a chemically guided generator of candidate configurations. The final machine-learned force fields are trained on high-fidelity MRSF-TDDFT labels; therefore, OM2/MRCI is required only to provide a qualitatively reasonable exploration of the relevant reactive basins, rather than quantitative accuracy. This requirement is supported by extensive prior applications of OM2/MRCI to excited-state topologies, conical intersections, and photoisomerization pathways in organic chromophores.[38−40,60−62] For chemical systems in which semiempirical dynamics fails to capture the relevant pathways even qualitatively, the present protocol can be naturally extended through active learning. In such a workflow, the initial OM2/MRCI trajectories would provide a baseline structural ensemble, which would then be labeled at the high-level ab initio or MRSF-TDDFT level to train a preliminary machine-learned force field. This coarse model could subsequently drive new nonadiabatic trajectories to explore regions of phase space inaccessible to OM2/MRCI, followed by iterative labeling, retraining, and refinement. Such an extension would further broaden the applicability of N^{2}ZND to systems with more complex electronic structures and less reliable semiempirical descriptions.

Although the present study focuses on gas-phase dynamics, an important future direction for the N^{2}ZND framework is its extension to complex chemical environments, such as solvents or polymer matrices, which can influence the operational behavior of molecular motors in practical applications. Analogous to conventional quantum mechanics/molecular mechanics (QM/MM) approaches, this extension could be realized through a hybrid machine learning/molecular mechanics (ML/MM) scheme.[63−65] In such a framework, the molecular motor would be described by the Allegro-based ML model, while the surrounding environment would be treated using a classical force field. Environmental electrostatic descriptors, such as the electric field at each atom of the motor, could be incorporated as additional input features following an environment-integrated embedding strategy.[64,66] During nonadiabatic dynamics, the MM engine would update the solvent coordinates and compute the instantaneous electrostatic descriptors, which would then be passed to the ML model together with the motor geometry to predict multistate energies and gradients. This ML/MM extension is naturally compatible with the Zhu−Nakamura surface hopping scheme used in N^{2}ZND, because the dynamics require only adiabatic energies and gradients rather than explicit nonadiabatic coupling vectors.

In conclusion, the integration of hierarchical sampling, equivariant deep learning, and NAC-free dynamics successfully bridges the long-standing gap between accuracy and efficiency in excited-state simulations. This framework transforms the study and design of light-driven molecular motors from a formidable computational challenge into a systematic and reliable predictive protocol. Ultimately, N^{2}ZND provides a rigorous and highly efficient blueprint, empowering the rational design and high-throughput computational screening of next-generation ultrafast molecular machines and responsive smart materials.

https://doi.org/10.1021/jacs.6c10141
J. Am. Chem. Soc. 2026, 148, 34758−34770

METHODS

Computational Details of *Ab Initio* Methods

The CASSCF method together with the 6−31G(d) basis set was used to optimize the ground-state equilibrium structures and the S_1/S_0 ConIs for CH_2NCH_3. The active space comprised six electrons distributed across six orbitals. For the DDIYM motor, the CASSCF calculations were performed with an active space of 12 electrons distributed across 12 orbitals. All CASSCF computations were carried out using the MOLPRO software package.[67,68]

Semiempirical calculations were performed at the OM2/MRCI level of theory using the implementation provided in the MNDO program.[69] The OM2/MRCI approach offers a favorable balance between computational efficiency and accuracy, making it particularly suitable for studying photoinduced processes in large molecular systems.[38−40] All energy and gradient evaluations required for geometry optimizations and dynamics simulations were carried out analytically. Self-consistent field (SCF) calculations were conducted within the restricted open-shell Hartree−Fock (ROHF) framework, as this formalism ensures a more appropriate representation of excited-state wave functions. The multireference configuration interaction (MRCI) expansion was constructed using three reference configurations: the closed-shell ground state configuration, along with single and double excitations from the highest occupied molecular orbital (HOMO) to the lowest unoccupied molecular orbital (LUMO). In the MRCI calculations, the active space comprises eight electrons distributed in eight orbitals. The ConIs geometries were located using the Lagrangian-Newton method.[70] To identify and track orbitals with π character and ensure the inclusion of π orbitals in the active space for bioinspired light-driven molecular rotary motor L-RSB, the π-type population (PIPOP) method was employed with a threshold value of 0.4.

The MRSF-TDDFT and SF-TDDFT calculations were carried out using the BH&HLYP hybrid functional in conjunction with the TZVP basis set, except for the computational efficiency benchmarks presented in Table 1, where the 6−31G(d,p) basis set was specifically employed. A ROHF reference wave function was employed, and empirical D3 dispersion corrections were incorporated to account for van der Waals interactions. The reference state for MRSF-TDDFT was constructed as an equiensemble of the $M_S = +1$ and $M_S = -1$ components of the triplet state, enabling a spin-adapted formalism within the linear response framework.[31−34] The reference state for the SF-TDDFT calculations was the pure $M_S = +1$ component of the triplet state. The ConIs geometries were located using the penalty function method.[71,72] The GAMESS-US program was utilized to carry out all the MRSF-TDDFT and SF-TDDFT calculations.[73,74]

Computational Details of Neural Network Training

The data set was constructed by combining Born−Oppenheimer molecular dynamics (BOMD) and Zhu−Nakamura NAMD simulations to capture structurally diverse configurations. Initial molecular geometries and corresponding velocities were generated using the Wigner sampling method based on ground-state vibrational frequencies.[51−53] For both BOMD and NAMD trajectories, the nuclear equations of motion were propagated numerically with the velocity Verlet algorithm, employing a fixed time step of 0.5 fs. All simulations were conducted at the OM2/MRCI level of theory. Structures were systematically extracted at intervals of 25−50 fs from each trajectory to ensure representative temporal sampling of the dynamical evolution. Detailed sampling procedures for CH_2NCH_3, the oxindole-based light-driven molecular rotary motor, and the bioinspired light-driven molecular rotary motor are provided in the Supporting Information.

The MLFF is constructed using Allegro,[41] configured with three layers, a maximum angular quantum number $l_{max} = 2$. The data set is randomly split into training and validation subsets at a 9:1 ratio. The initial learning rate is set to 0.001 and subsequently reduced using an on-plateau scheduler with a patience of 50 and a decay factor of 0.5. The model is trained with a joint mean square error loss function that simultaneously optimizes per-atom energies and forces, utilizing the Adam optimizer. Training terminates when the learning rate drops below 10^{-5}.

Computational Details of NAMD Calculations

The nonadiabatic photoisomerization dynamics was examined employing trajectory surface-hopping simulations utilizing the Zhu−Nakamura theoretical framework.[42−44] Nuclear equations of motion were propagated numerically via the velocity Verlet algorithm using a fixed time step of 0.5 fs. An energy gap criterion of 0.5 eV was employed.

ASSOCIATED CONTENT

Data Availability Statement

The source code for the N²ZND framework developed in this study is fully open-source and freely available. The repository features the Zhu−Nakamura surface hopping dynamics module, which is interfaced with MNDO2020 (for OM2/MRCI), GAMESS-US (for MRSF-TDDFT), and Allegro Neural Networks. Additionally, the package includes implementations of the Hierarchical On-the-Fly Sampling strategy and structural optimization algorithms, as well as the scripts used for interpolation and Multidimensional Scaling (MDS) analysis. The code can be accessed on GitHub at https://github.com/JianzhengMa/n2znd.git.

Supporting Information

The Supporting Information is available free of charge at https://pubs.acs.org/doi/10.1021/jacs.6c10141.

Supporting text, tables, and figures detailing the theoretical frameworks (MRSF-TDDFT, Zhu−Nakamura dynamics, Allegro model, and structural optimization algorithms); sampling protocols and multidimensional scaling (MDS) analysis; MLFF training metrics, optimized geometrical parameters, excited-state decay kinetics, and representative trajectory evolutions for CH_2NCH_3, DDIYM, L-RSB, and Me-L-RSB; validation of MRSF/ZNSH against MRSF/FSSH for CH_2NCH_3; comparison of ab initio and MLFF potential energy curves for the DDIYM and L-RSB motors; dihedral angle distributions near $S_1 \rightarrow S_0$ hopping points for the DDIYM motor; temperature-dependent kinetics and hopping distributions for the L-RSB motor; and schematic potential energy profiles, vertical excitation energies, and synthetic feasibility discussion for the rationally designed Me-L-RSB motor (PDF)

Raw data for figures; structure and trajectory files for this work (ZIP)

AUTHOR INFORMATION

Corresponding Author

Weibin Chu − *Key Laboratory for Computational Physical Sciences (MOE), State Key Laboratory of Surface Physics, Institute of Computational Physical Sciences and Department of Physics, Fudan University, Shanghai 200433, China;* orcid.org/0000-0001-5951-0337; Email: wbchu@fudan.edu.cn

Authors

Jianzheng Ma − *Key Laboratory for Computational Physical Sciences (MOE), State Key Laboratory of Surface Physics, Institute of Computational Physical Sciences and Department of Physics, Fudan University, Shanghai 200433, China*

Chenwei Jiang − *Ministry of Education Key Laboratory for Nonequilibrium Synthesis and Modulation of Condensed Matter, Shaanxi Province Key Laboratory of Quantum Information and Quantum Optoelectronic Devices, School of Physics, Xi' An Jiaotong University, Xi'an 710049, China*
Lei Peng − *Key Laboratory for Computational Physical Sciences (MOE), State Key Laboratory of Surface Physics, Institute of Computational Physical Sciences and Department of Physics, Fudan University, Shanghai 200433, China*
Yongliang Shi − *Key Laboratory for Computational Physical Sciences (MOE), State Key Laboratory of Surface Physics, Institute of Computational Physical Sciences and Department of Physics, Fudan University, Shanghai 200433, China*
Yingzhou Li − *School of Mathematical Sciences, Fudan University, Shanghai 200433, China;* orcid.org/0000-0003-1852-3750
Zhenggang Lan − *SCNU Environmental Research Institute, Guangdong Provincial Key Laboratory of Chemical Pollution and Environmental Safety & MOE Key Laboratory of Environmental Theoretical Chemistry, South China Normal University, Guangzhou 510006, China;* orcid.org/0000-0002-8509-0388
Oleg V. Prezhdo − *Department of Chemistry and Department of Physics & Astronomy, University of Southern California, Los Angeles, California 90089, United States*
Xin-Gao Gong − *Key Laboratory for Computational Physical Sciences (MOE), State Key Laboratory of Surface Physics, Institute of Computational Physical Sciences and Department of Physics, Fudan University, Shanghai 200433, China*

Complete contact information is available at: https://pubs.acs.org/10.1021/jacs.6c10141

Notes

The authors declare no competing financial interest.

■ ACKNOWLEDGMENTS

We thank Prof. Chaoyuan Zhu for fruitful discussions. W.B.C. acknowledges the support of the National Key Research and Development Program of China (grant no. 2024YFA1409800); NSFC (grant nos. 12188101, 12274081, and 22203016); Shanghai Pilot Program for Basic Research—Fudan University 21TQ1400100 (grant no. 22TQ017). X.G.G. acknowledges the support of the Innovation Program for Quantum Science and Technology (grant no. 2024ZD0300100). O.V.P. acknowledges the support of the US National Science Foundation (grant no. CHE-2603101). Z.G.L. acknowledges the support of the NSFC (grant nos. 22333003 and 22361132528).

■ REFERENCES

(1) Erbas-Cakmak, S.; Leigh, D. A.; McTernan, C. T.; Nussbaumer, A. L. Artificial Molecular Machines. *Chem. Rev.* **2015**, *115*, 10081−10206.
(2) Groppi, J.; Baroncini, M.; Venturi, M.; Silvi, S.; Credi, A. Design of photo-activated molecular machines: highlights from the past ten years. *Chem. Commun.* **2019**, *55*, 12595−12602.
(3) Baroncini, M.; Silvi, S.; Credi, A. Photo- and Redox-Driven Artificial Molecular Motors. *Chem. Rev.* **2020**, *120*, 200−268.
(4) Pooler, D. R. S.; Lubbe, A. S.; Crespi, S.; Feringa, B. L. Designing light-driven rotary molecular motors. *Chem. Sci.* **2021**, *12*, 14964−14986.
(5) Sheng, J.; Danowski, W.; Sardjan, A. S.; Hou, J.; Crespi, S.; Ryabchun, A.; Domínguez, M. P.; Jan Buma, W.; Browne, W. R.; Feringa, B. L. Formylation boosts the performance of light-driven overcrowded alkene-derived rotary molecular motors. *Nat. Chem.* **2024**, *16*, 1330−1338.
(6) Greb, L.; Lehn, J.-M. Light-Driven Molecular Motors: Imines as Four-Step or Two-Step Unidirectional Rotors. *J. Am. Chem. Soc.* **2014**, *136*, 13114−13117.
(7) Tully, J. C. Molecular dynamics with electronic transitions. *J. Chem. Phys.* **1990**, *93*, 1061−1071.
(8) Hammes-Schiffer, S.; Tully, J. C. Proton transfer in solution: Molecular dynamics with quantum transitions. *J. Chem. Phys.* **1994**, *101*, 4657−4667.
(9) Granucci, G.; Persico, M. Critical appraisal of the fewest switches algorithm for surface hopping. *J. Chem. Phys.* **2007**, *126*, 134114.
(10) Fabiano, E.; Groenhof, G.; Thiel, W. Approximate switching algorithms for trajectory surface hopping. *Chem. Phys.* **2008**, *351*, 111−116.
(11) Fabiano, E.; Keal, T.; Thiel, W. Implementation of surface hopping molecular dynamics using semiempirical methods. *Chem. Phys.* **2008**, *349*, 334−347.
(12) Westermayr, J.; Marquetand, P. Machine Learning for Electronically Excited States of Molecules. *Chem. Rev.* **2021**, *121*, 9873−9926.
(13) Mai, S.; González, L. Molecular Photochemistry: Recent Developments in Theory. *Angew. Chem. Int. Ed.* **2020**, *59*, 16832−16846.
(14) Gruber, E.; Kabylda, A. M.; Nielsen, M. B.; Rasmussen, A. P.; Teiwes, R.; Kusochek, P. A.; Bochenkova, A. V.; Andersen, L. H. Light Driven Ultrafast Bioinspired Molecular Motors: Steering and Accelerating Photoisomerization Dynamics of Retinal. *J. Am. Chem. Soc.* **2022**, *144*, 69−73.
(15) Li, J.; Lopez, S. A. A Look Inside the Black Box of Machine Learning Photodynamics Simulations. *Acc. Chem. Res.* **2022**, *55*, 1972−1984.
(16) Bachmair, B.; Reiner, M. M.; Tiefenbacher, M. X.; Marquetand, P. *Chemical Modelling*; The Royal Society of Chemistry, 2022; pp. 178−200.
(17) Chen, W.-K.; Liu, X.-Y.; Fang, W.-H.; Dral, P. O.; Cui, G. Deep Learning for Nonadiabatic Excited-State Dynamics. *J. Phys. Chem. Lett.* **2018**, *9*, 6702−6708.
(18) Hu, D.; Xie, Y.; Li, X.; Li, L.; Lan, Z. Inclusion of Machine Learning Kernel Ridge Regression Potential Energy Surfaces in On-the-Fly Nonadiabatic Molecular Dynamics Simulation. *J. Phys. Chem. Lett.* **2018**, *9*, 2725−2732.
(19) Westermayr, J.; Gastegger, M.; Menger, M. F. S. J.; Mai, S.; González, L.; Marquetand, P. Machine learning enables long time scale molecular photodynamics simulations. *Chem. Sci.* **2019**, *10*, 8100−8107.
(20) Ha, J.-K.; Kim, K.; Min, S. K. Machine Learning-Assisted Excited State Molecular Dynamics with the State-Interaction State-Averaged Spin-Restricted Ensemble-Referenced Kohn-Sham Approach. *J. Chem. Theory Comput.* **2021**, *17*, 694−702.
(21) Li, J.; Reiser, P.; Boswell, B. R.; Eberhard, A.; Burns, N. Z.; Friederich, P.; Lopez, S. A. Automatic discovery of photoisomerization mechanisms with nanosecond machine learning photodynamics simulations. *Chem. Sci.* **2021**, *12*, 5302−5314.
(22) Mausenberger, S.; Müller, C.; Tkatchenko, A.; Marquetand, P.; González, L.; Westermayr, J. SPAINN: equivariant message passing for excited-state nonadiabatic molecular dynamics. *Chem. Sci.* **2024**, *15*, 15880−15890.
(23) Moon, S. W.; Willow, S. Y.; Park, T. H.; Min, S. K.; Myung, C. W. Machine Learning Nonadiabatic Dynamics: Eliminating Phase Freedom of Nonadiabatic Couplings with the State-Interaction State-Averaged Spin-Restricted Ensemble-Referenced Kohn-Sham Approach. *J. Chem. Theory Comput.* **2025**, *21*, 1521−1529.
(24) Martinka, J.; Zhang, L.; Hou, Y.-F.; Martyka, M.; Pittner, J.; Barbatti, M.; Dral, P. O. A Descriptor Is All You Need: Accurate Machine Learning of Nonadiabatic Coupling Vectors. *J. Phys. Chem. Lett.* **2025**, *16*, 11732−11744.

(25) Wang, Z.; Dong, J.; Qiu, J.; Wang, L. All-Atom Nonadiabatic Dynamics Simulation of Hybrid Graphene Nanoribbons Based on Wannier Analysis and Machine Learning. *ACS Appl. Mater. Interfaces* **2022**, *14*, 22929−22940.
(26) Shakiba, M.; Akimov, A. V. Machine-Learned Kohn-Sham Hamiltonian Mapping for Nonadiabatic Molecular Dynamics. *J. Chem. Theory Comput.* **2024**, *20*, 2992−3007.
(27) Zhang, C.; Zhong, Y.; Tao, Z.-G.; Qin, X.; Shang, H.; Lan, Z.; Prezhdo, O. V.; Gong, X.-G.; Chu, W.; Xiang, H. Advancing nonadiabatic molecular dynamics simulations in solids with E(3) equivariant deep neural hamiltonians. *Nat. Commun.* **2025**, *16*, 2033.
(28) Cao, B.; Dong, J.; Wang, Z.; Wang, L. Large-Scale Non-Adiabatic Dynamics Simulation Based on Machine Learning Hamiltonian and Force Field: The Case of Charge Transport in Monolayer MoS2. *J. Phys. Chem. Lett.* **2025**, *16*, 4907−4920.
(29) Li, S.; Xie, B.-B.; Yin, B.-W.; Liu, L.; Shen, L.; Fang, W.-H. Construction of Highly Accurate Machine Learning Potential Energy Surfaces for Excited-State Dynamics Simulations Based on Low-Level Data Sets. *J. Phys. Chem. A* **2024**, *128*, 5516−5524.
(30) Martyka, M.; Zhang, L.; Ge, F.; Hou, Y.-F.; Jankowska, J.; Barbatti, M.; Dral, P. O. Charting electronic-state manifolds across molecules with multi-state learning and gap-driven dynamics via efficient and robust active learning. *Npj Comput. Mater.* **2025**, *11*, 132.
(31) Lee, S.; Filatov, M.; Lee, S.; Choi, C. H. Eliminating spin-contamination of spin-flip time dependent density functional theory within linear response formalism by the use of zeroth-order mixed-reference (MR) reduced density matrix. *J. Chem. Phys.* **2018**, *149*, 104101.
(32) Lee, S.; Kim, E. E.; Nakata, H.; Lee, S.; Choi, C. H. Efficient implementations of analytic energy gradient for mixed-reference spin-flip time-dependent density functional theory (MRSF-TDDFT). *J. Chem. Phys.* **2019**, *149*, 104101.
(33) Komarov, K.; Park, W.; Lee, S.; Zeng, T.; Choi, C. H. Accurate Spin-Orbit Coupling by Relativistic Mixed-Reference Spin-Flip-TDDFT. *J. Chem. Theory Comput.* **2023**, *19*, 953−964.
(34) Park, W.; Lee, S.; Komarov, K.; Mironov, V.; Nakata, H.; Zeng, T.; Huix-Rotllant, M.; Choi, C. H. MRSF-TDDFT: A new tool in quantum chemistry for better understanding molecules and materials. *Bull. Korean Chem. Soc.* **2025**, *46*, 330−346.
(35) Shao, Y.; Head-Gordon, M.; Krylov, A. I. The spin-flip approach within time-dependent density functional theory: Theory and applications to diradicals. *J. Chem. Phys.* **2003**, *118*, 4807−4818.
(36) Weber, W.; Thiel, W. Orthogonalization corrections for semiempirical methods. *Theor. Chem. Acc.* **2000**, *103*, 495−506.
(37) Koslowski, A.; Beck, M. E.; Thiel, W. Implementation of a general multireference configuration interaction procedure with analytic gradients in a semiempirical context using the graphical unitary group approach. *J. Comput. Chem.* **2003**, *24*, 714−726.
(38) Dral, P. O.; Wu, X.; Spörkel, L.; Koslowski, A.; Thiel, W. Semiempirical Quantum-Chemical Orthogonalization-Corrected Methods: Benchmarks for Ground-State Properties. *J. Chem. Theory Comput.* **2016**, *12*, 1097−1120.
(39) Wang, Y.; Liu, X.; Cui, G.; Fang, W.; Thiel, W. Photoisomerization of Arylazopyrazole Photoswitches: Stereospecific Excited-State Relaxation. *Angew. Chem. Int. Ed.* **2016**, *55*, 14009−14013.
(40) Cui, G.; Lan, Z.; Thiel, W. Intramolecular Hydrogen Bonding Plays a Crucial Role in the Photophysics and Photochemistry of the GFP Chromophore. *J. Am. Chem. Soc.* **2012**, *134*, 1662−1672.
(41) Musaelian, A.; Batzner, S.; Johansson, A.; Sun, L.; Owen, C. J.; Kornbluth, M.; Kozinsky, B. Learning local equivariant representations for large-scale atomistic dynamics. *Nat. Commun.* **2023**, *14*, 579.
(42) Kondorskiy, A.; Nakamura, H. Semiclassical theory of electronically nonadiabatic chemical dynamics: Incorporation of the Zhu-Nakamura theory into the frozen Gaussian propagation method. *J. Chem. Phys.* **2004**, *120*, 8937−8954.
(43) Yu, L.; Xu, C.; Lei, Y.; Zhu, C.; Wen, Z. Trajectory-based nonadiabatic molecular dynamics without calculating nonadiabatic coupling in the avoided crossing case: trans ↔cis photoisomerization in azobenzene. *Phys. Chem. Chem. Phys.* **2014**, *16*, 25883−25895.
(44) Ishida, T.; Nanbu, S.; Nakamura, H. Clarification of nonadiabatic chemical dynamics by the Zhu-Nakamura theory of nonadiabatic transition: from tri-atomic systems to reactions in solutions. *Int. Rev. Phys. Chem.* **2017**, *36*, 229−285.
(45) Roke, D.; Sen, M.; Danowski, W.; Wezenberg, S. J.; Feringa, B. L. Visible-Light-Driven Tunable Molecular Motors Based on Oxindole. *J. Am. Chem. Soc.* **2019**, *141*, 7622−7627.
(46) Pooler, D. R. S.; Pierron, R.; Crespi, S.; Costil, R.; Pfeifer, L.; Léonard, J.; Olivucci, M.; Feringa, B. L. Effect of charge-transfer enhancement on the efficiency and rotary mechanism of an oxindole-based molecular motor. *Chem. Sci.* **2021**, *12*, 7486−7497.
(47) Ma, J.; Zhao, D.; Yu, L.; Jiang, C.; Lan, Z.; Li, F. Simultaneously improving the efficiencies of photo- and thermal isomerization of an oxindole-based light-driven molecular rotary motor by a structural redesign. *Phys. Chem. Chem. Phys.* **2023**, *25*, 12800−12809.
(48) Vuković, L.; Burmeister, C. F.; Král, P.; Groenhof, G. Control Mechanisms of Photoisomerization in Protonated Schiff Bases. *J. Phys. Chem. Lett.* **2013**, *4*, 1005−1011.
(49) Agrafiotis, D. K.; Rassokhin, D. N.; Lobanov, V. S. Multidimensional scaling and visualization of large molecular similarity tables. *J. Comput. Chem.* **2001**, *22*, 488−500.
(50) Andreella, A.; De Santis, R.; Vesely, A.; Finos, L. Procrustes-based distances for exploring between-matrices similarity. *Statistical Methods Appl.* **2023**, *32*, 867−882.
(51) Wigner, E. On the Quantum Correction For Thermodynamic Equilibrium. *Phys. Rev.* **1932**, *40*, 749−759.
(52) Barbatti, M.; Sen, K. Effects of different initial condition samplings on photodynamics and spectrum of pyrrole. *Int. J. Quantum Chem.* **2016**, *116*, 762−771.
(53) Zobel, J. P.; Nogueira, J. J.; González, L. Finite-temperature Wigner phase-space sampling and temperature effects on the excited-state dynamics of 2-nitronaphthalene. *Phys. Chem. Chem. Phys.* **2019**, *21*, 13906−13915.
(54) Mai, S.; Marquetand, P.; González, L. Nonadiabatic dynamics: The SHARC approach. *WIREs Comput. Mol. Sci.* **2018**, *8*, No. e1370.
(55) Mai, S.; Avagliano, D.; Heindl, M.; Marquetand, P.; Menger, M. F. S. J.; Oppel, M.; Plasser, F.; Polonius, S.; Ruckenbauer, M.; Shu, Y.; et al. *SHARC3.0: Surface Hopping Including Arbitrary CouplingsProgram Package for Non-Adiabatic Dynamics*; Zenodo, 2023. DOI: .
(56) Kazaryan, A.; Lan, Z.; Schäfer, L. V.; Thiel, W.; Filatov, M. Surface Hopping Excited-State Dynamics Study of the Photoisomerization of a Light-Driven Fluorene Molecular Rotary Motor. *J. Chem. Theory Comput.* **2011**, *7*, 2189−2199.
(57) Bitzek, E.; Koskinen, P.; Gähler, F.; Moseler, M.; Gumbsch, P. Structural Relaxation Made Simple. *Phys. Rev. Lett.* **2006**, *97*, 170201.
(58) Stecher, T.; Reuter, K.; Oberhofer, H. First-Principles Free-Energy Barriers for Photoelectrochemical Surface Reactions: Proton Abstraction at TiO_2(110). *Phys. Rev. Lett.* **2016**, *117*, 276001.
(59) Ma, J.; Zhao, D.; Jiang, C.; Lan, Z.; Li, F. Effect of Temperature on Photoisomerization Dynamics of a Newly Designed Two-Stroke Light-Driven Molecular Rotary Motor. *Int. J. Mol. Sci.* **2022**, *23*, 9694.
(60) Weingart, O.; Lan, Z.; Koslowski, A.; Thiel, W. Chiral Pathways and Periodic Decay in cis-Azobenzene Photodynamics. *J. Phys. Chem. Lett.* **2011**, *2*, 1506−1509.
(61) Gámez, J. A.; Weingart, O.; Koslowski, A.; Thiel, W. Cooperating Dinitrogen and Phenyl Rotations in trans-Azobenzene Photoisomerization. *J. Chem. Theory Comput.* **2012**, *8*, 2352−2358.
(62) Nikiforov, A.; Gamez, J. A.; Thiel, W.; Filatov, M. Computational Design of a Family of Light-Driven Rotary Molecular Motors with Improved Quantum Efficiency. *J. Phys. Chem. Lett.* **2016**, *7*, 105−110.
(63) Wang, L.; Li, J. Modeling the Nonradiative Decay of Cyclooctatetrathiophene in Solution and Crystal Phases Using Machine Learning. *J. Chem. Theory Comput.* **2025**, *21*, 9300−9308.
(64) Tiefenbacher, M. X.; Bachmair, B.; Chen, C. G.; Westermayr, J.; Marquetand, P.; Dietschreit, J. C. B.; González, L. Excited-state

nonadiabatic dynamics in explicit solvent using machine learned interatomic potentials. *Digital Discovery* **2025**, *4*, 1478−1491.
(65) Grassano, J. S.; Pickering, I.; Roitberg, A. E.; Estrin, D. A.; Semelak, J. A. From QM/MM to ML/MM: A new era in multiscale modeling. *Chem. Phys. Rev* **2025**, *6*, 041304.
(66) Gastegger, M.; Schütt, K. T.; Müller, K.-R. Machine learning of solvent effects on molecular spectra and reactions. *Chem. Sci.* **2021**, *12*, 11473−11483.
(67) Werner, H.-J., et al.. *MOLPRO, version 2019.1, a package of ab initio programs*, 2019.
(68) Werner, H.; Knowles, P. J.; Knizia, G.; Manby, F. R.; Schütz, M. Molpro: a general-purpose quantum chemistry program package. *WIREs Comput. Mol. Sci.* **2012**, *2*, 242−253.
(69) Thiel, W. *MNDO program, version 8.0*. Max-Planck-Institut für Kohlenforschung: Mülheim. 2019.
(70) Keal, T. W.; Koslowski, A.; Thiel, W. Comparison of algorithms for conical intersection optimization using semiempirical methods. *Theor. Chem. Acc.* **2007**, *118*, 837−844.
(71) Levine, B. G.; Martínez, T. J. Isomerization Through Conical Intersections. *Annu. Rev. Phys. Chem.* **2007**, *58*, 613−634.
(72) Levine, B. G.; Ko, C.; Quenneville, J.; Martínez, T. J. Conical intersections and double excitations in time-dependent density functional theory. *Mol. Phys.* **2006**, *104*, 1039−1051.
(73) Schmidt, M. W.; Baldridge, K. K.; Boatz, J. A.; Elbert, S. T.; Gordon, M. S.; Jensen, J. H.; Koseki, S.; Matsunaga, N.; Nguyen, K. A.; Su, S.; Windus, T. L.; Dupuis, M.; Montgomery, J. A. General atomic and molecular electronic structure system. *J. Comput. Chem.* **1993**, *14*, 1347−1363.
(74) Gordon, M. S.; Schmidt, M. W. *Theory and Applications of Computational Chemistry, the first forty years*, Dykstra, C. E.; Frenking, G.; Kim, K. S.; Scuseria, G. E.; Eds. Elsevier: Amsterdam, 2005; Vol. *41*, pp. 1167−1189.

https://doi.org/10.1021/jacs.6c10141
J. Am. Chem. Soc. 2026, 148, 34758−34770